



Geophysical Research Letters

RESEARCH LETTER

10.1029/2019GL084787

Key Points:

- Rotary shear test under micro-CT measures frictional behavior and shows progressive development of slip induced fractures
- Fracture surface area estimated by machine learning aided quantitative image analysis
- Fracture energy accounts for ~16% of the total energy budget, among which <2% is consumed by creating off-fault fractures

Supporting Information:

- Supporting Information S1

Correspondence to:

Q. Zhao,
q.zhao@mail.utoronto.ca

Citation:

Zhao, Q., Glaser, S. D., Tisato, N., & Grasselli, G. (2020). Assessing energy budget of laboratory fault slip using rotary shear experiments and micro-computed tomography. *Geophysical Research Letters*, 47, e2019GL084787. <https://doi.org/10.1029/2019GL084787>

Received 30 JUL 2019

Accepted 24 DEC 2019

Accepted article online 3 JAN 2020

Assessing Energy Budget of Laboratory Fault Slip Using Rotary Shear Experiments and Micro-Computed Tomography

Qi Zhao¹, Steven D. Glaser¹, Nicola Tisato^{2,3}, and Giovanni Grasselli³

¹Department of Civil and Environmental Engineering, University of California, Berkeley, CA, USA, ²Department of Geological Sciences, Jackson School of Geosciences, The University of Texas at Austin, Austin, TX, USA, ³Department of Civil and Mineral Engineering, University of Toronto, Toronto, Ontario, Canada

Abstract Quantitative assessment of the energy budget of earthquake events is one of the key aspects for understanding the physics of earthquakes. Investigation of laboratory fault slips under controlled conditions can provide insights on this important aspect of the natural and induced earthquakes. We conducted a rotary shear experiment under X-ray micro-computed tomography, which allowed in situ and operando measurement of macroscopic stresses and imaging of the newly formed fractures inside the sample. We estimate each component of the energy budget and found that friction energy loss (E_F), fracture energy (E_G), and radiated energy (E_R) account for 70.16%, 15.68%, and 14.15% of the total energy budget, respectively. Quantitative analysis of the micro-computed tomography images indicates that the energy consumed by creating slip-induced off-fault fractures (E_G^f) accounts for only 0.3% of the total energy, less than 2% of the total E_G .

1. Introduction

During an earthquake, the accumulated potential energy, which includes elastic strain energy (E_s) and gravitational energy (E_g), is partially released. The released potential energy (ΔW) is partitioned into friction energy loss (E_F), fracture energy (E_G), and radiated energy (E_R) (Kanamori & Heaton, 2000):

$$\Delta W = E_F + E_G + E_R. \quad (1)$$

The energy budget of earthquakes has been investigated by a large body of research (e.g., Aubry et al., 2018; Brantut & Viesca, 2017; Chester et al., 2005; Kanamori & Heaton, 2000; McBeck et al., 2019; McGarr, 1999; Nielsen et al., 2016; Passelègue et al., 2016; Scholz, 1990; Wilson et al., 2005; Yoshioka, 1986).

Despite extensive investigations, studies regarding the relative amount of energy consumed by fracturing, E_G , are inconclusive. Field studies inferred E_G ranges from <1% to >50% of the total released energy (e.g., Chester et al., 2005; Wilson et al., 2005), while laboratory experiments and theoretical models suggest much smaller values at 0.01–0.1% of the total released energy (e.g., Scholz, 1990; Yoshioka, 1986). The disagreement about the relative size of E_G is related to the difficulty in assessing the fracture surface area, which includes surface area of cataclastic particles, surface area of gouge particles, and surface area of microfractures, all of which may exist in a broad damage zone bounding the fault (Chester et al., 2005). Quantitative assessment of the energy consumed by co-seismic processes can provide critical information on the dynamic stress conditions of the earthquakes, improving our understanding of earthquake physics including rupture mechanisms and propagation speed, energy budget, and gouge formation (Di Toro et al., 2005).

Over the last several decades, X-ray micro-computed tomography (micro-CT) has been increasingly used to investigate microscopic structures of geomaterials (e.g., Ketcham & Carlson, 2001; Renard et al., 2004; Tatone & Grasselli, 2015), and the state-of-art in this research area evolved from examining post-mortem specimen (i.e., remove tested specimen from the testing facility and scan) to in situ and operando observations (e.g., Renard et al., 2017; Tisato et al., 2016; Zhao, 2017; Zhao et al., 2017; Zhao et al., 2018). The recently developed ERDμ-T rotary shear testing facility that is paired with X-ray micro-CT allows observations of the gradual variation within the tested sample after each incremental slip step (Zhao et al., 2017). This apparatus has been used to conduct a series of laboratory fault slip tests and gain intriguing insights of the gradual fault

evolution and development of off-fault fractures (Zhao et al., 2018). In this study, we improve our comprehension of the data collected in Zhao et al. (2018) by quantitatively assessing the energy budget of the laboratory fault slips.

2. Materials and Methods

2.1. Rotary Shear Test Under Micro-CT

The experiment is set up and performed using the ERDμ-T apparatus following the steps described by Zhao et al. (2017) and Zhao et al. (2018) (Figure 1a). Here for completeness, we briefly summarize the experimental setup and procedure. The tested specimen is a cylindrical flowstone (microfine calcium sulfate cement mortar) sample 12 mm in diameter and 32 mm in length. The specimen is divided into top and bottom semisamples by three-point bending, which created two matching rough surfaces representing the hanging and foot walls of the laboratory fault (Figure 1b).

The test is conducted in an unconfined condition with an initial nominal normal stress of 2.5 MPa. The top semisample is then rotated incrementally against the bottom semisample, which is fixed to the load-and-torque cell, for two 3° steps and four 6° steps, that is, Rot. I to VI (Figure 1c). During each slip step, the top semisample is accelerated to the velocity of 3°/s in 0.1 s and stopped almost instantaneously at the desired distance. Normal force and torque are recorded during rotation and used to calculate friction coefficient (μ). After each incremental slip of 6°, we conduct a 3-D micro-CT scan. The small slip step size allows for imaging of the gradual morphological evolution of the sample.

2.2. Micro-CT Scan and Image Data Analysis

Each micro-CT scan generates a 3-D digital volume that consists of subvolumes (i.e., voxels) possessing grayscale values that are, as a first approximation, proportional to material density at the corresponding spatial locations. We segment the digital volume into two phases based on the grayscale values: solid (i.e., specimen) and void (i.e., fractures and pores). This segmentation process is critical to the accuracy of further quantitative analysis. The segmentation results by manual thresholding in Zhao et al. (2018) provide qualitative observations of the fracture development in the tested sample. To ensure accuracy of further quantitative analysis, we compare four additional segmentation methods including conventional segmentation approaches using isodata algorithm, k -means clustering, and region growing (Adams & Bischof, 1994; Jain & Dubes, 1988; Ridler & Calvard, 1978), and a recently developed machine learning image segmentation method. The former three methods are automated based on the statistical features of the grayscale values of voxels. The machine learning image segmentation is performed using a random forest classifier trained using manually labeled images. It extracts 33 features using various filters as input and performs pixel-wise classification (supporting information Text S1, Figure S1, and Tables S1–S5).

After segmentation, we examine different surfaces and their areas in the sample volume (Figure 2). We divide the total surface area of the sample (A_t) into three components: (i) the initial surface area (A_i), which includes the outer surface area of the sample, the initial fractured surface area, and the surface of the hole in the top semisample; (ii) the noncontacting surface area on the shear surface (A_{nc}); and (iii) the shear-induced secondary fracture surface area (A_f).

The total surface area in the sample volume (A_t) is estimated by counting the voxels belonging to all the surface boundaries, which is calculated as the difference between the sample volume and the morphologically eroded sample volume (Gonzalez & Woods, 2002; Zhao, 2017).

The noncontacting surface area on the shear surface, A_{nc} can be calculated from the nominal contact area (A_n) and A_c using

$$A_{nc}=2(A_n-A_c), \quad (2)$$

where the multiplier 2 accounts for the fact that we are considering top and bottom sides of the noncontacting surface. The real contact area (A_c) is calculated following the method in Zhao et al. (2018).

At the initial condition, A_t is divided into A_{nc} and A_i :

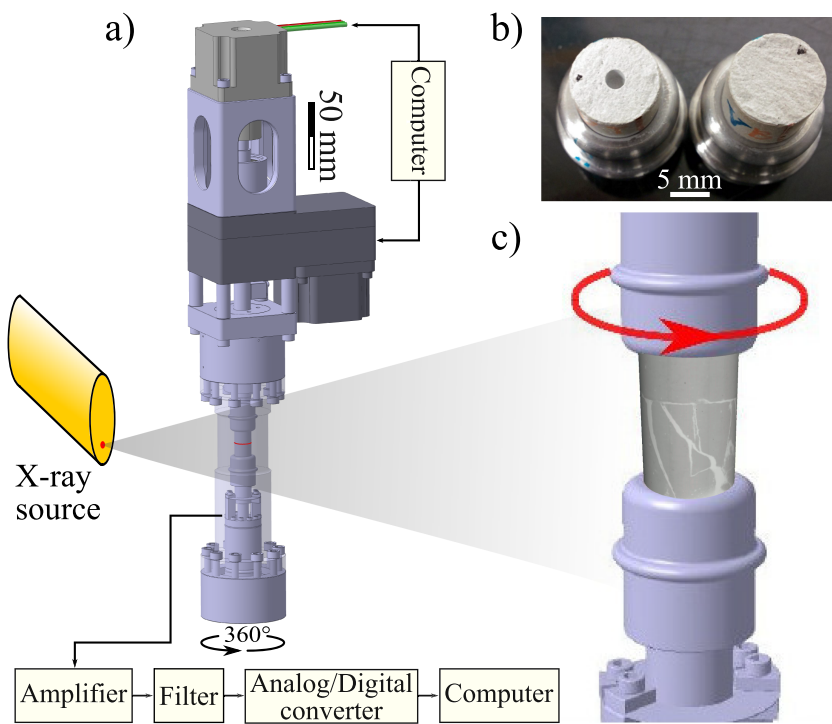


Figure 1. Schematic illustration of the ERDμ-T experiment setup. (a) The ERDμ-T vessel placed inside the X-ray μ CT machine, mounted on the CNC rotation stage. (b) The top (left) and bottom (right) semisamples. (c) Zoom-in view of the sample during a test.

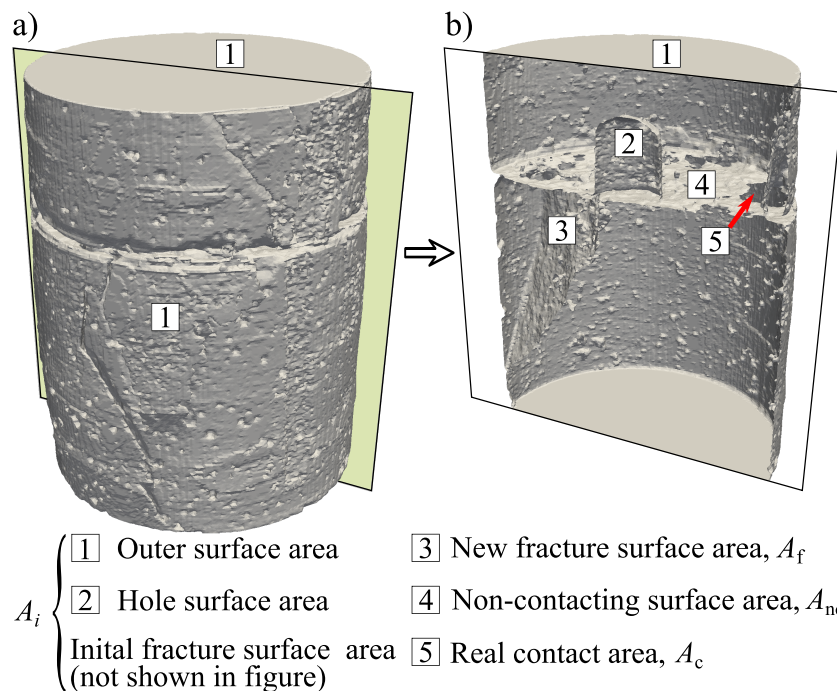


Figure 2. (a, b) Three-dimensional rendering views illustrating different types of surface areas in the sample volume. The image data after Rot. III is taken as an example.

$$A_t = A_{nc} + A_i, \quad (3)$$

and we consider A_i to be constant throughout the experiment.

For the successive rotation steps, shear-induced fractures form, and the area of these newly formed fractures (A_f) is also a part of A_t :

$$A_t = A_f + A_{nc} + A_i. \quad (4)$$

Thus, A_f can be assessed using

$$A_f = A_t - A_i - A_{nc}, \quad (5)$$

and the fracture area created in each rotation step (ΔA_f) is simply computed as the difference of A_f between two consecutive steps.

2.3. Energy Budget

In the laboratory shear experiment the energy input (W_I) is mainly from the rotary motor. Thus, the energy budget of the laboratory fault slip can be written as follows:

$$\Delta W + W_I = E_F + E_G + E_R. \quad (6)$$

The left-hand side of equation (6) can be calculated from measured macroscopic static stress change and torque during slipping. Numerous models have been used to estimate the right-hand side of equation (6), and we use the commonly used slip weakening (SW) model (Ida, 1972; Kanamori & Heaton, 2000). According to this model, the local shear stress decreases from the peak value (τ_p) to a constant residual stress (τ_r) as the slip increases to the critical slip distance (D_c), and further slip occurs with shear stress at the residual level.

- i The energy release (ΔW) is from the gravitational energy change (ΔE_g) and the elastic energy change (ΔE_s) in the sample: $\Delta W = -(\Delta E_s + \Delta E_g)$, that is, increase of energy stored in the sample results in decrease of energy released to the faulting process. The center of gravity of the sample is not vertically translated during the experiment; therefore, we neglected ΔE_g . We further divided ΔE_s into the change in elastic energy due to normal load change (ΔE_s^n) and torque change (ΔE_s^t), and they are calculated using static (i.e., before and after each slip) normal force and torque measurements (Parrish & Camm, 1973):

$$\Delta E_s^n = \frac{(N_r^2 - N_i^2)L}{2EA_n}, \quad (7)$$

$$\Delta E_s^t = \frac{(M_r^2 - M_i^2)L}{2GJ}, \quad (8)$$

where N_i and N_r are the normal force measured at the start and the end of the rotation, M_i and M_r are the corresponding torque measurements, L is the total sample length, E is the Young's modulus, A_n is the nominal contact area, G is the shear modulus that can be estimated through E and Poisson's ratio (ν) by $G = E/(2(1 + \nu))$, and J is the polar moment of inertia ($J = \pi R^4/2$, where R is the sample radius). The strain energy variation due to the elastic deformation of the apparatus is also estimated using equations (7) and (8) (supporting information Text S2).

- ii The mechanical energy input (W_I) is calculated from the torque (M) and the angular shear distance (Ω) (Kleppner & Kolenkow, 2013):

$$W_I = \int_0^\Omega M d\Omega. \quad (9)$$

- iii The friction energy loss (E_F) is estimated using the residual shear stress (τ_r), the averaged slip distance (u), and the nominal fault surface area (A_n) (Kanamori & Heaton, 2000):

$$E_F = A_n \int_0^u \tau_r du. \quad (10)$$

where $0 < u \leq D_t$ and D_t is the total averaged slip distance.

- iv The fracture energy (E_G) can be estimated using the shear stress measured during slipping (τ) (Kanamori & Heaton, 2000):

$$E_G = A_n \int_0^u \tau - \tau_r du, \quad (11)$$

where $0 < u \leq D_c$ and D_c is inferred from the SW model. The energy required to create new fracture surfaces (E_G^f) can be assessed from the newly created surface area (ΔA_f). Observations from micro-CT images suggest that these are tensile fractures (mode I) created due to the interlocking and breakdown of asperities (Zhao et al., 2018); thus, the mode I fracture energy (G_{lc}) is used to calculate the fracture surface energy using Griffith theory of brittle fracture (Griffith, 1920):

$$E_G^f = \frac{\Delta A_f}{2} G_{lc}, \quad (12)$$

where half of the new fracture surface area is considered for the fact that fractures have two identical sides.

- v The radiated energy (E_R) can be considered as the remaining portion of the total energy (E_T) from the SW model using (Kanamori & Heaton, 2000)

$$E_R = E_T - E_F - E_G, \quad (13)$$

where

$$E_T = A_n \int_0^u \tau_T du, \quad (14)$$

and τ_T decreases linearly from τ_p to τ_r with u increasing from 0 to D_t . This model indicates that when the stress drop is sudden, there is significant radiated energy, and when the stress drop is gradual, there is minimal radiated energy (Kanamori & Heaton, 2000).

3. Results

Due to the application of the initial normal force, a fracture develops axially (Figure 3a). During rotation steps Rot. I and II, the initial fracture opens and propagates, causing the bottom semisample to split, and this process corresponds to the significant drop of frictional resistance at the end of Rot. I (Figure 3b). During Rot. III, a fracture forms in the center of the bottom semisample, and two fractures form close to the periphery of the top semisample (Figure 3c). During Rot. IV, a small fracture forms at the bottom semisample, connecting the two fractures formed in the earlier steps (Figure 3d). No observable fractures form in Rot. V and VI (Figures 3e and 3f).

The frictional behavior (excluding the initial 0.16-mm ramp-up phase in Rot. I) can be described by a linear SW model (Figure 3g) (Zhao et al., 2018), with the following parameters: $\tau_p = 4.44$ MPa, to $\tau_r = 2.40$ MPa, $D_c = 0.82$ mm, and $D_t = 1.56$ mm. After the experiment, the sample is removed from the apparatus and opened, and a thin layer of powder (i.e., gouge) is observed on the slipping surface (Figure 3h).

The fracture surface area (A_f) estimated from micro-CT image data using different algorithms show a similar trend (Figure 4, see details in the supporting information Tables S1–S5). In general, A_f increased as a function of slip distance, indicating more shear-induced fractures. However, A_f values decrease slightly at the last slip step, except for the result from the machine learning method, which shows that A_f plateaus after Rot. IV. The decrease of A_f shown by conventional segmentation methods may be attributed to the close of fractures due to the sample movement and that conventional segmentation methods are not able to capture fractures with small apertures. The machine learning aided image segmentation provides a more plausible depiction of the variation of fracture surface area, as it depicts concealed fractures better than other methods. Thus, we proceed to energy analysis using this result.

The total energy (E_T) calculated from static stress measurement and torque ($\Delta W + W_I$) is 537.71 mJ, and the total energy estimated from the SW model ($E_F + E_G + E_R$) is 567.33 mJ (Figures 5a and 5b). This shows the applicability of the SW model (see detailed breakdown of the energy budget in the supporting information Table S6). The SW model shows that for the entire slip distance, E_F , E_G , and E_R account for 70.16%, 15.68%, and 14.15% of E_T , respectively. Therefore, the seismic radiation efficiency $\eta_R = E_R / (E_R + E_G)$ is 0.47.

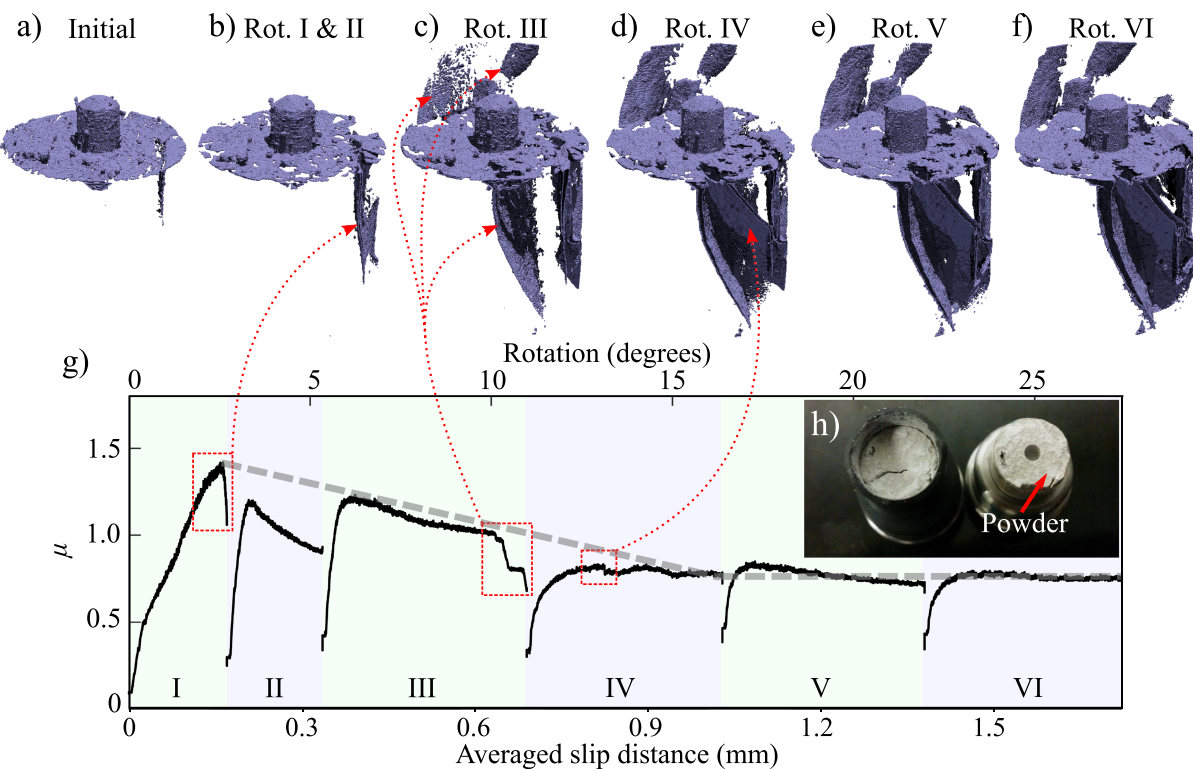


Figure 3. (a–f) Three-dimensional rendering of the laboratory fault surface and shear-induced fractures at the initial condition and after each $\sim 6^\circ$ incremental slip (Rot. I to VI). (g) Friction coefficient as a function of averaged slip distance for Rot. I to VI. Red dotted boxes and arrows highlight sudden friction drops that correspond to formation of off-fault fractures. The dashed gray line represents the slip weakening model (after Zhao et al., 2018). (h) Laboratory fault surface observed after the experiment. Note the fine powder layer partially covering the fault surface.

The total fracture energy (E_G) inferred from the SW model is 88.98 mJ; in contrast, the energy consumed by creating secondary off-fault fractures (E_G^f) is 1.72 mJ. E_G^f accounts for only 0.30% of E_T and 1.92% of E_G . In specific energy terms, the specific fracture energy (E_G/A_n) is 836.93 J/m², and the specific fracture surface energy (E_G^f/A_n) is 16.15 J/m²; both of them increase with increasing slipping distance before the critical slip distance and plateau afterward (Figure 5c).

4. Discussion

The linear SW model adequately describes the overall frictional behavior. However, E_T is significantly smaller than $\Delta W + W_I$ at the first slip step, and the discrepancy decreases with the increasing slip distance. This suggests that the simple linear SW model is not capturing the complex stress variation at the initial portion of the faulting process, likely due to the relatively rough fault surface. In our laboratory experiment, the faulting involves both dynamic and quasistatic processes: the rapid shear stress drop because of the breakage of large asperities and creation of large fractures is a dynamic process that radiates relatively large E_R , and the fault movement at the imposed slip velocity with the shear stress gradually decreasing is a quasistatic process that radiates negligible E_R .

The relative percentages of E_F , E_G , and E_R agree with laboratory results by McBeck et al. (2019). The radiation efficiency $\eta_R = 0.47$ aligns with the values for the laboratory experiments (e.g., Passelègue et al., 2016) and shallow earthquakes (Nishitsui & Mori, 2013). However, note that we

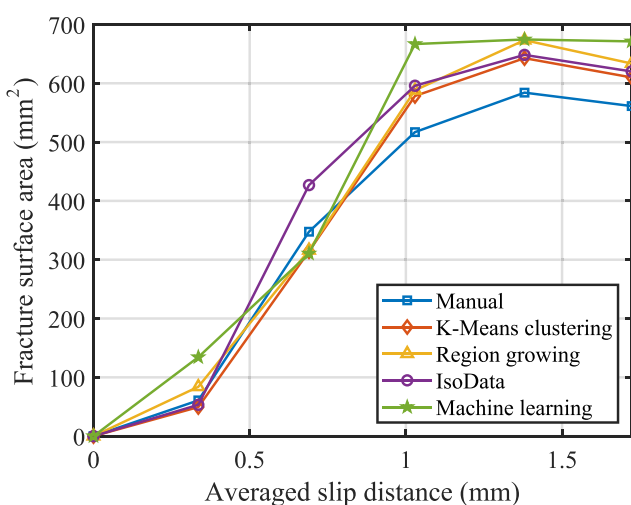


Figure 4. Estimation of surface area of shear-induced new fractures by different image segmentation methods including manual thresholding, k -means clustering, region growing, isodata algorithm, and machine learning method.

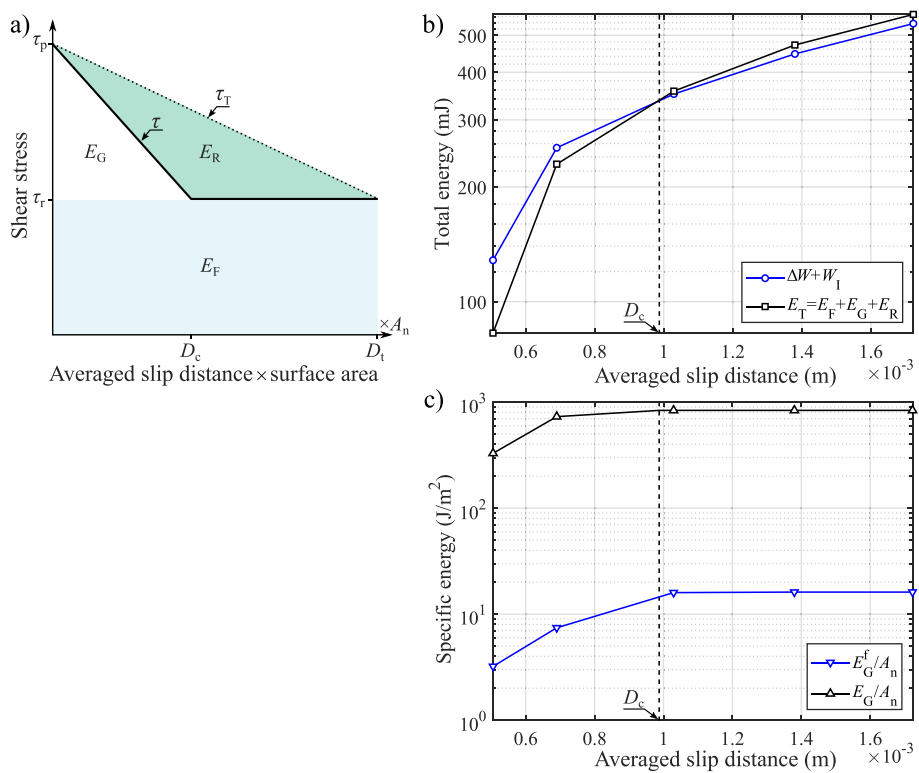


Figure 5. (a) The linear slip weakening model. (b) Total energy budget calculated from static stress and torque measurement ($\Delta W + W_1$) and the SW model (E_T). (c) Variation of specific fracture energy (E_G/A_n) and specific fracture surface energy (E_G^f/A_n).

conduct the experiment under a relatively low initial normal stress of 2.5 MPa, and the shear stress drop (~ 2 MPa) is larger than those observed on experiments conducted on saw cut planes and estimated for shallow earthquakes. Such a large stress drop could be justified by the fact that our laboratory fault is rougher than other experiments. The relatively high surface roughness causes increase of D_c and $\tau_p - \tau_r$ (Okubo & Dieterich, 1984), which increases the E_G . As a result, the specific fracture energy at the scale of 10^2 – 10^3 J/m 2 is higher than values reported from saw cut plane slip experiments under similar stress conditions at 10^{-2} to 10^2 J/m 2 (Nielsen et al., 2016; Ohnaka, 2003; Okubo & Dieterich, 1981; Passelègue et al., 2016) but lower than that of intact rocks at 10^4 J/m 2 (Ohnaka, 2003).

Secondary fracturing alongside the main fault is observed among a wide range of scales, in forms of, for example, secondary faults, en echelon fractures and injection veins of pseudotachylites, which introduce important energy sinks (Belardinelli et al., 2000; Di Toro et al., 2005; Savage & Brodsky, 2011). With the careful quantitative estimation of fracture surface area from the micro-CT images, we estimate that the energy used to create secondary off-fault fractures (E_G^f) accounts for only 0.30% of the total energy budget, quantitatively agree with the study of Chester et al. (2005). Note that we interpret the off-fault secondary fractures as tensile fractures (mode I). These oblique to subvertical fractures form because of stress concentration on asperities, which may be important in shallow earthquakes (Dalguer et al., 2003).

Examination of the post-mortem sample shows a thin layer of fine powder (i.e., gouge) that covers part of the fault surface. The grain size of this powder layer is below the resolution of the micro-CT imaging (i.e., 25 μ m), and the gouge material is lost when removing the sample from the testing vessel after the experiment. Therefore, a quantitative assessment of the actual grain surface area of the fault gouge is not possible. However, it is reasonable to presume that the in-fault damage, which includes grain crushing, grinding, and other mechanical processes as the fault slips, may account for the rest >98% of E_G . In future studies, gouge material could be collected, so we can measure the volume of pulverized material, and scanning electron microscope could be used to obtain the actual particle size.

Our results suggest that shear-induced tensile fractures may have large extent at shallow depth (i.e., low confinement) but consumes negligible energy. In contrast, energy dissipation related to a dynamic slip pulse may also create off-fault damage (Rice et al., 2005) and may pulverize the fault zone rocks, in some cases consuming 50% or more of the total energy budget (Wilson et al., 2005). Our laboratory observations help to reconcile discrepancies on fracture energy estimations.

5. Conclusion

We use the ERD μ -T apparatus to conduct rotary shear experiments under the micro-CT, which allows measurement of macroscopic stress and inspection of the tested sample interior at incremental slip steps without introducing undesired perturbations. In our experiment, E_F , E_G , and E_R account for 70.16%, 15.68%, and 14.15% of the total energy, respectively. The machine learning aided quantitative micro-CT image analysis demonstrates that energy required to create tensile off-fault secondary fractures consumes a little portion (<2%) of the total fracture energy, and most fracture energy is contributed to in-fault damaging processes. These laboratory observations may help to link microscopic and macroscopic fracturing processes to the energy budget obtained in structural geology, rock mechanics, and seismology, improving our understanding of earthquake physics.

Acknowledgments

This work is funded by the National Science Foundation (award 005400). We would like to thank the editor, Dr. Ben Holtzman, Dr. Florian Amann, and the anonymous reviewers for their review and constructive suggestions. Raw image and mechanical measurement data (~7 GB) can be accessed in the following links: <https://128.100.14.241/owncloud/index.php/s/bTbasfJbwfDjOwD> <https://128.100.14.241/owncloud/index.php/s/Gv9CdVcPQxRBx5m>.

References

- Adams, R., & Bischof, L. (1994). Seeded region growing. *IEEE Transactions on Pattern Analysis and Machine Intelligence*, 16(6), 641–647. <https://doi.org/10.1109/34.295913>
- Aubry, J., Passelègue, F. X., Deldicque, D., Girault, F., Marty, S., Lahfid, A., et al. (2018). Frictional heating processes and energy budget during laboratory earthquakes. *Geophysical Research Letters*, 45, 12–274. <https://doi.org/10.1029/2018gl079263>
- Belardinelli, M. E., Bonafede, M., & Gudmundsson, A. (2000). Secondary earthquake fractures generated by a strike-slip fault in the South Iceland Seismic Zone. *Journal of Geophysical Research*, 105(B6), 13,613–13,629. <https://doi.org/10.1029/2000JB900058>
- Brantut, N., & Viesca, R. C. (2017). The fracture energy of ruptures driven by flash heating. *Geophysical Research Letters*, 44, 6718–6725. <https://doi.org/10.1002/2017GL074110>
- Chester, J. S., Chester, F. M., & Kronenberg, A. K. (2005). Fracture surface energy of the Punchbowl fault, San Andreas system. *Nature*, 437(7055), 133–136. <https://doi.org/10.1038/nature03942>
- Dalguer, L. A., Irikura, K., & Riera, J. D. (2003). Simulation of tensile crack generation by three-dimensional dynamic shear rupture propagation during an earthquake. *Journal of Geophysical Research*, 108(B3), 2144. <https://doi.org/10.1029/2001JB001738>
- Di Toro, G., Nielsen, S., & Pennacchioni, G. (2005). Earthquake rupture dynamics frozen in exhumed ancient faults. *Nature*, 436(7053), 1009–1012. <https://doi.org/10.1038/nature03910>
- Gonzalez, R. C., & Woods, R. E. (2002). *Digital image processing*. Upper Saddle River, New Jersey: Prentice-Hall Inc.
- Griffith, A. A. (1920). The phenomena of rupture and flow in solids. *Philosophical Transactions of the Royal Society of London. Series A, Containing Papers of a Mathematical or Physical Character*, 221(582–593), 163–198. <https://doi.org/10.1098/rsta.1921.0006>
- Ida, Y. (1972). Cohesive force across the tip of a longitudinal shear crack and Griffith's specific surface energy. *Journal of Geophysical Research*, 77(20), 3796–3805. <https://doi.org/10.1029/JB077i020p03796>
- Jain, A. K., & Dubes, R. C. (1988). *Algorithms for clustering data*. Upper Saddle River: Prentice Hall.
- Kanamori, H., & Heaton, T. H. (2000). Microscopic and macroscopic physics of earthquakes. In J. B. Rundle, D. L. Turcotte, & W. Klein (Eds.), *GeoComplexity and the Physics of Earthquakes* (Vol. 120, pp. 147–164). Washington, DC: Geophysical Monograph-American Geophysical Union.
- Ketcham, R. A., & Carlson, W. D. (2001). Acquisition, optimization and interpretation of X-ray computed tomographic imagery: Applications to the geosciences. *Computers & Geosciences*, 27(4), 381–400. [https://doi.org/10.1016/s0098-3004\(00\)00116-3](https://doi.org/10.1016/s0098-3004(00)00116-3)
- Kleppner, D., & Kolenkow, R. (2013). *An introduction to mechanics*. Cambridge: Cambridge University Press.
- McBeck, J., Cordonnier, B., Mair, K., & Renard, F. (2019). The evolving energy budget of experimental faults within continental crust: Insights from in situ dynamic X-ray microtomography. *Journal of Structural Geology*, 123, 42–53. <https://doi.org/10.1016/j.jsg.2019.03.005>
- McGarr, A. (1999). On relating apparent stress to the stress causing earthquake fault slip. *Journal of Geophysical Research*, 104(B2), 3003–3011. <https://doi.org/10.1029/1998JB900083>
- Nielsen, S., Spagnuolo, E., Smith, S., Violay, M., Di Toro, G., & Bistacchi, A. (2016). Scaling in natural and laboratory earthquakes. *Geophysical Research Letters*, 43, 1504–1510. <https://doi.org/10.1002/2015GL067490>
- Nishitsuji, Y., & Mori, J. (2013). Source parameters and radiation efficiency for intermediate-depth earthquakes in Northeast Japan. *Geophysical Journal International*, 196(2), 1247–1259. <https://doi.org/10.1093/gji/ggt458>
- Ohnaka, M. (2003). A constitutive scaling law and a unified comprehension for frictional slip failure, shear fracture of intact rock, and earthquake rupture. *Journal of Geophysical Research*, 108(B2), 2080. <https://doi.org/10.1029/2000JB000123>
- Okubo, P. G., & Dieterich, J. H. (1981). Fracture energy of stick-slip events in a large scale biaxial experiment. *Geophysical Research Letters*, 8(8), 887–890. <https://doi.org/10.1029/GL008i008p00887>
- Okubo, P. G., & Dieterich, J. H. (1984). Effects of physical fault properties on frictional instabilities produced on simulated faults. *Journal of Geophysical Research*, 89(B7), 5817–5827. <https://doi.org/10.1029/JB089iB07p05817>
- Parrish, A., & Camm, F. J. (1973). *Mechanical engineer's reference book*. London: Butterworths.
- Passelègue, F., Schubnel, A., Nielsen, S., Bhat, H. S., Deldicque, D., & Madariaga, R. (2016). Dynamic rupture processes inferred from laboratory microearthquakes. *Journal of Geophysical Research: Solid Earth*, 121, 4343–4365. <https://doi.org/10.1002/2015JB012694>
- Renard, F., Bernard, D., Thibault, X., & Boller, E. (2004). Synchrotron 3D microtomography of halite aggregates during experimental pressure solution creep and evolution of the permeability. *Geophysical Research Letters*, 31, L07607. <https://doi.org/10.1029/2004GL019605>

- Renard, F., Cordonnier, B., Kobchenko, M., Kandula, N., Weiss, J., & Zhu, W. (2017). Microscale characterization of rupture nucleation unravels precursors to faulting in rocks. *Earth and Planetary Science Letters*, 476, 69–78. <https://doi.org/10.1016/j.epsl.2017.08.002>
- Rice, J. R., Sammis, C. G., & Parsons, R. (2005). Off-fault secondary failure induced by a dynamic slip pulse. *Bulletin of the Seismological Society of America*, 95(1), 109–134. <https://doi.org/10.1785/0120030166>
- Ridler, T. W., & Calvard, S. (1978). Picture thresholding using an iterative selection method. *IEEE Transactions on Systems, Man, and Cybernetics*, 8, 630–632.
- Savage, H. M., & Brodsky, E. E. (2011). Collateral damage: Evolution with displacement of fracture distribution and secondary fault strands in fault damage zones. *Journal of Geophysical Research*, 116, B03405. <https://doi.org/10.1029/2010JB007665>
- Scholz, C. H. (1990). *The mechanics of earthquakes and faulting*. Cambridge: Cambridge University Press.
- Tatone, B. S., & Grasselli, G. (2015). Characterization of the effect of normal load on the discontinuity morphology in direct shear specimens using X-ray micro-CT. *Acta Geotechnica*, 10(1), 31–54. <https://doi.org/10.1007/s11440-014-0320-5>
- Tisato, N., Zhao, Q., & Grasselli, G. (2016). Experimental rock physics under micro-CT. *SEG Technical Program Expanded Abstracts*, 2016, 3251–3255.
- Wilson, B., Dewers, T., Reches, Z., & Brune, J. (2005). Particle size and energetics of gouge from earthquake rupture zones. *Nature*, 434(7034), 749–752. <https://doi.org/10.1038/nature03433>
- Yoshioka, N. (1986). Fracture energy and the variation of gouge and surface roughness during frictional sliding of rocks. *Journal of Physics of the Earth*, 34(4), 335–355. <https://doi.org/10.4294/jpe1952.34.335>
- Zhao, Q. (2017). Investigating brittle rock failure and associated seismicity using laboratory experiments and numerical simulations, PhD thesis, PhD thesis, University of Toronto.
- Zhao, Q., Tisato, N., & Grasselli, G. (2017). Rotary shear experiments under X-ray micro-computed tomography. *The Review of Scientific Instruments*, 88(1), 015110. <https://doi.org/10.1063/1.4974149>
- Zhao, Q., Tisato, N., Kovaleva, O., & Grasselli, G. (2018). Direct observation of faulting by means of rotary shear tests under X-ray micro-computed tomography. *Journal of Geophysical Research: Solid Earth*, 123, 7389–7403. <https://doi.org/10.1029/2017jb015394>